

RocMLMs: Predicting Rock Properties through Machine Learning Models

Buchanan Kerswell ¹Nestor Cerpa ¹Andréa Tommasi ¹Marguerite Godard

¹José Alberto Padrón-Navarta ²

⁵Géosciences Montpellier, Université de Montpellier & CNRS, Montpellier, France

⁶Instituto Andaluz de Ciencias de la Tierra, CSIC–UGR, Granada, Spain

Key Points:

- RocMLMs predict rock properties up to 10^1 – 10^3 faster than commonly used methods
- RocMLMs trained with Neural Networks are more efficient compared to other regression algorithms
- RocMLM training data show good agreement with PREM and STW105 for an average mantle geotherm

14 **Abstract**

15 Mineral phase transformations significantly alter the bulk density and elastic properties
16 of mantle rocks and consequently have profound effects on mantle dynamics and seis-
17 mic wave propagation. These changes in the physical properties of mantle rocks result
18 from evolution in the equilibrium mineralogical composition, which can be predicted by
19 the minimization of the Gibbs Free Energy with respect to pressure (P), temperature
20 (T), and chemical composition (X). Thus, numerical models that simulate mantle con-
21 vection and/or probe the elastic structure of the Earth's mantle must account for vary-
22 ing mineralogical compositions to be self-consistent. Yet coupling Gibbs Free Energy min-
23 imization (GFEM) approaches with numerical geodynamic models is currently intractable
24 for high-resolution simulations because execution speeds of widely-used GFEM programs
25 (10^0 – 10^2 ms) are impractical in many cases. As an alternative, this study introduces ma-
26 chine learning models (RocMLMs) that have been trained to predict thermodynamically
27 self-consistent rock properties at arbitrary PTX conditions between 1–28 GPa, 773–2273
28 K, and mantle compositions ranging from fertile (lherzolitic) to refractory (harzburgitic)
29 end-members defined with a large dataset of published mantle compositions. RocMLMs
30 are 10^1 – 10^3 times faster than GFEM calculations or GFEM-based look-up table approaches
31 with equivalent accuracy. Depth profiles of RocMLMs predictions are nearly indistin-
32 guishable from reference models PREM and STW105, demonstrating good agreement
33 between thermodynamic-based predictions of density, Vp, and Vs and geophysical ob-
34 servations. RocMLMs are therefore capable, for the first time, of emulating dynamic evo-
35 lution of density, Vp, and Vs in high-resolution numerical geodynamic models.

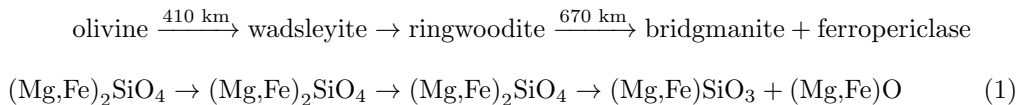
36 **Plain language summary**

37 The mineralogical makeup of rocks within Earth's mantle largely determines how the
38 mantle flows over geologic time, and how it responds to seismic waves triggered by earth-
39 quakes, because mineral assemblages control important rock properties such as density
40 and stiffness (elasticity). The mineralogy of mantle rocks is not constant, however. It
41 changes depending on three factors: pressure, temperature, and the chemical composi-
42 tion of the rock. Thus, it is important for computer simulations of mantle convection to
43 account for the evolution of rock mineralogy. Computer programs that can predict rock
44 properties based on thermodynamic calculations are available, but are generally too slow
45 to be used in high-resolution simulations. As an alternative approach, this study intro-

duces machine learning models (RocMLMs) that have “learned” how to predict rock properties (density and elasticity) by “training” on a large dataset of thermodynamic calculations. We demonstrate that RocMLMs can then predict rock properties up to 10^1 – 10^3 times faster than state-of-the-art methods. We tested RocMLM predictions against reference mantle models based on observations of seismic waves and found good agreement. RocMLMs are therefore capable of fast and highly-accurate predictions of changes in rock properties and can be implemented in high-resolution computer simulations of mantle convection.

1 Introduction

The dominant mineral phases in Earth’s mantle are olivine, pyroxene, garnet, wadsleyite, ringwoodite, bridgmanite, ferropericlase, calcium silicate perovskite, and MgSiO_3 post-perovskite (e.g., Stixrude and Lithgow-Bertelloni, 2012). Mantle mineralogy evolves with depth by a series of relatively discontinuous phase transformations that define sharp transitions in the physical properties of mantle rocks (Ringwood, 1991). The most important phase transformations occur at depths between 410 km and 670 km beneath Earth’s surface, defining the transition from the upper to the lower mantle (Equation (1)). This mantle transition zone (MTZ) is characterized by sharp variations in density and elastic properties that strongly impact mantle convection (Christensen, 1995; Fukao et al., 2001; Jenkins et al., 2016; Karato et al., 2001; Kuritani et al., 2019; Nakagawa and Buffett, 2005; Ringwood, 1991; Schubert et al., 1975; Tackley et al., 1994; Wang et al., 2015), and the propagation of teleseismic waves (Dziewoński and Anderson, 1981; Ita and Stixrude, 1992; Ringwood, 1991). The MTZ is therefore an essential feature for modeling mantle structure and dynamics. With respect to a simple FeO-MgO-SiO₂ chemical system, the most important MTZ reactions can be written as:



These phase changes (e.g., Equation (1)) are often parameterized in numerical geodynamic simulations with simple pressure-temperature (PT)-dependent reaction boundaries based on high-pressure experiments (e.g., Agrusta et al., 2017; Ballmer et al., 2015;

73 Christensen, 1995; Čížková and Bina, 2013; Kerswell et al., 2021; Liu et al., 1991; Nak-
74 agawa and Buffett, 2005; Tackley et al., 1994; Torii and Yoshioka, 2007). Alternatively,
75 some numerical geodynamic experiments (e.g., Li et al., 2019; Yang and Faccenda, 2020)
76 use Gibbs Free Energy minimization (GFEM) programs (e.g., Connolly, 2009; Riel et al.,
77 2022) to precompute Lookup Tables of rock properties, which are subsequently referenced
78 to adjust material properties as the numerical experiments evolve. These implementa-
79 tions usually consider fixed ideal mantle compositions, such as pyrolite, and/or approx-
80 imate phase transitions with simple functions. These approaches neglect the PT depen-
81 dency of mineral transitions on natural variations of mantle composition (X) such as vari-
82 ations of Fe-Mg and Al-Ca that may be either primordial or result from melt extraction
83 or reactions during melt transport. Despite these simplifications, these models have cor-
84 roborated that the MTZ is a critical feature impacting subduction dynamics, mantle plume
85 dynamics, and water cycling in the deep Earth.

86 More self-consistent numerical models of mantle convection would track changes
87 in physical properties of mantle rocks by computing GFEM as a function of the evolu-
88 tion of PTX conditions. However, this is currently intractable for high-resolution geo-
89 dynamic models because GFEM programs remain too slow ($\geq 4\text{--}228$ ms per PTX point)
90 to be applied recursively during a geodynamic simulation (see Supporting Information).
91 Parallelization of GFEM programs can increase efficiency by scaling the number of par-
92 allel processes (Riel et al., 2022), but continuously computing phase relations during geo-
93 dynamic simulations would require GFEM efficiency on the order of $\leq 10^0\text{--}10^{-1}$ ms to
94 be feasible (see Supporting Information), which may be difficult to achieve solely by par-
95 allelisation and/or direct improvements to the current GFEM paradigm.

96 Here, we propose an alternative approach to predicting rock properties based on
97 the use of machine learning models (referred to as RocMLMs) that have been “trained”
98 on a multidimensional dataset of precomputed rock properties using classical (k-Neighbors,
99 Decision Trees) and deep (Neural Network) regression algorithms. These later regres-
100 sion algorithms compress large amounts of thermodynamic information into highly ef-
101 ficient nonlinear functions, allowing RocMLMs to infer (predict) rock properties across
102 arbitrary PTX conditions faster than any current GFEM algorithm. We demonstrate
103 that RocMLMs are thus highly efficient emulators of GFEM programs and are well-suited
104 for predicting bulk rock properties in numerical geodynamic models.

This article begins by detailing our method for building, training, and evaluating RocMLMs. We then demonstrate that RocMLMs can predict densities and seismic velocities in a dry upper mantle and transition zone up to 10^1 – 10^3 times faster than commonly used GFEM programs with equivalent accuracies. Finally, we compare RocMLM predictions with reference models derived from seismological datasets (Dziewoński and Anderson, 1981; Kustowski et al., 2008) and discuss the accuracy and performance of RocMLMs with respect to their future implementation in numerical geodynamic models.

2 Methods

The following sections describe the methodologies employed in constructing, training, and assessing RocMLMs, with a focus on four primary objectives. First, define the size and scope of RocMLM training data to ensure widespread applicability of RocMLMs to the upper mantle and transition zone (Section 2.1). Second, define a generalized approach for generating RocMLM training data to ensure applicability to any GFEM program (e.g., MAGEMin, Perple_X, and others, Section 2.2). Third, train RocMLMs on a set of input features that can be routinely computed during geodynamic simulations to ensure widespread applicability of RocMLMs to various geodynamic codes (Section 2.3). Fourth, rank the overall performance of RocMLMs in terms of accuracy and efficiency (Section 2.4).

2.1 RocMLM Training Dataset Design

2.1.1 Pressure-Temperature Conditions

High-pressure experiments constrain the reaction olivine \rightarrow wadsleyite between 14.0 ± 1.0 GPa and 1600 ± 400 K with Clapeyron slopes between $2.4 \times 10^{-3} \pm 1.4 \times 10^{-3}$ GPa/K (Akaogi et al., 1989; Katsura and Ito, 1989; Li et al., 2019; Morishima et al., 1994). Likewise, the reaction ringwoodite \rightarrow bridgemanite + ferropericlase is constrained between 24.0 ± 1.5 GPa and 1600 ± 400 K with negative Clapeyron slopes between $-2.0 \times 10^{-3} \pm 1.6 \times 10^{-3}$ GPa/K (Akaogi et al., 2007; Bina and Helffrich, 1994; Hirose, 2002; Ishii et al., 2018; Ito, 1982; Ito et al., 1990; Ito and Katsura, 1989; Ito and Takahashi, 1989; Katsura et al., 2003; Litasov et al., 2005). We therefore compute RocMLM training data within a rectangular PT region bounded between 1–28 GPa and 773–2273 K to encompass ex-

135 pected conditions for the entire upper mantle and MTZ—from approximately 30 km to
 136 865 km depth (Figure 1).

137 Figure 1 shows that our training dataset PT range includes PT conditions that are
 138 not expected to exist in either the Earth’s mantle, nor geodynamic simulations (e.g.,
 139 very cold conditions with thermal gradients ≤ 5 K/km, Cerpa et al., 2022; Maruyama
 140 et al., 1996; Syracuse et al., 2010). Such a large rectangular PT range might be consid-
 141 ered impractical with respect to training efficiency (unnecessary amounts of training data)
 142 and accuracy (outside the bounds of calibrated thermodynamic data) compared to an
 143 irregular PT range bounded between arbitrary geotherms. However, initial sensitivity
 144 tests showed comparable RocMLM performance irrespective of the range of PT condi-
 145 tions used to generate RocMLM training data. Thus, we adopted a regular rectangu-
 146 lar training dataset design because it is computationally convenient and does not dete-
 147 riorate RocMLM accuracy.

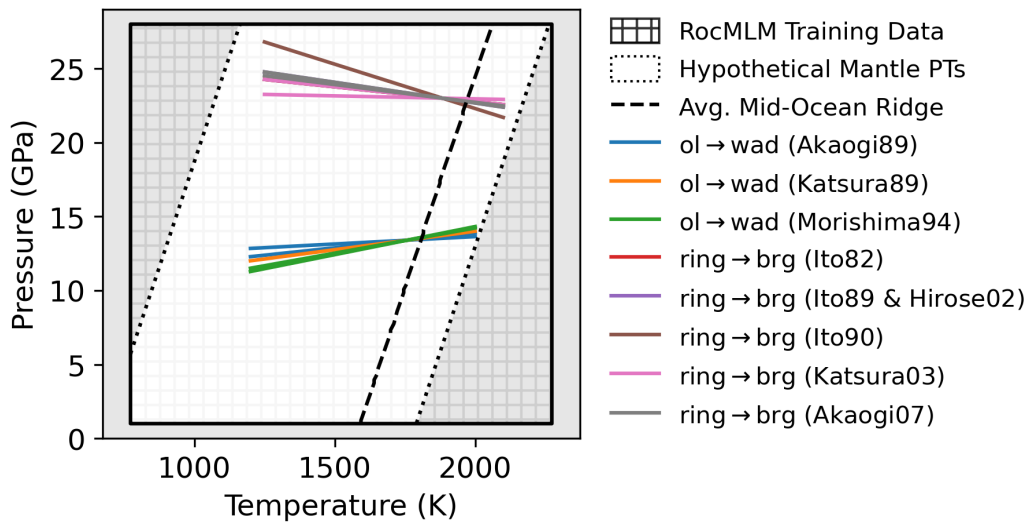


Figure 1: PT diagram showing the range of conditions considered for generating RocMLM training data (hatched region) compared to a range of possible upper mantle conditions (inner white region). The dotted black lines are geotherms with arbitrary mantle potential temperatures of 673 K and 1773 K and a constant adiabatic gradient of 0.5 K/km, representing hypothetical lower and upper bounds for mantle PT conditions (including hypothetical cold lithospheric slabs). The dashed black line is an average geotherm for a mid-ocean ridge (1573 K adiabat). Phase boundaries for the 410 km and 670 km discontinuities (colored lines) are from a compilation by Li et al. (2019).

148 **2.1.2 Bulk Mantle Compositions**

149 We derived an array of synthetic bulk mantle compositions with the aim of encom-
 150 passing the widest range of chemical variability in Earth's mantle. For this, we applied
 151 a statistical analysis to publicly-available geochemical data from thousands of natural
 152 peridotite samples. The procedure was as follows.

153 Bulk chemical analyses of peridotite samples were downloaded using the Earthchem.org
 154 Search Portal with a single search criterion: “*set sample type > igneous rocks > names*
 155 *from Earthchem categories > igneous-plutonic-ultramafic*”. The search queried 19791 sam-
 156 ples with rock type classifications that we did not modify from their original labels. Sam-
 157 ples lacking analyses for SiO₂, MgO, Al₂O₃, or CaO were excluded from the dataset. All
 158 samples classified as “unknown”, chromitite, limburgite, wehrlite, undifferentiated peri-
 159 dotite, dunite, or pyroxenite were also excluded from the dataset to focus on samples that
 160 are most likely mantellic, that is, residues of partial melting modified (or not) by refer-
 161 tilization, rather than products of fractional crystallization (Bowen, 1915). The data were
 162 grouped according to the remaining rock types (lherzolite and harzburgite) and outliers
 163 were removed from each group using a 1.5 interquartile range threshold applied to each
 164 chemical component. Cr and Ni measured as minor elements (ppm) were converted to
 165 Cr₂O₃ and NiO (wt.%) and all Fe oxides were converted to Fe₂O₃T. Total oxides were
 166 then checked against H₂O, CO₂, and LOI to determine if chemical analyses were per-
 167 formed before or after ignition. Analyses with total oxides summing to $\leq 97\%$ or $\geq 103\%$
 168 were considered erroneous, or otherwise low-quality, and excluded from the dataset. All
 169 analyses were then normalized to a volatile-free basis before converting Fe₂O₃T to FeOT.
 170 After normalization, the final compositional space investigated includes the components
 171 Na₂O-CaO-FeO-MgO-Al₂O₃-SiO₂-TiO₂ (NCFMAST system). The final dataset contains
 172 3111 chemical analyses of classified peridotite samples (Table 1).

173 We applied Principal Component Analysis (PCA) to the standardized peridotite
 174 dataset to reduce its dimensionality from the original 7-oxides space. PCA requires com-
 175 plete data, so samples were first arranged by decreasing MgO and increasing SiO₂ con-
 176 tent and a k-Neighbors algorithm was applied to impute missing oxide analyses, which
 177 were mainly the Na₂O component (see Table 1 for missing analyses counts). Following
 178 common practice, a “z-score normalization” was applied to all oxide components before
 179 running PCA. The first two principal components (PC1 and PC2) explain 78% of the

180 variance of the dataset, which we considered to be sufficient for modeling a broad range
 181 of peridotitic mantle compositions. PC1 separates samples by their TiO₂, Al₂O₃, MgO,
 182 CaO, and Na₂O contents, while PC2 separates samples by SiO₂ and FeO (Figure 2).

183 In this PC space, we drew a mixing line connecting the lherzolite and harzburgite
 184 group centroids (i.e., the median values for PC1 and PC2 for each group). The lherzolite-
 185 harzburgite mixing line was then extended until reaching the approximate location of
 186 the most fertile (Al₂O₃-CaO-TiO₂-rich) and most refractory (MgO-rich, SiO₂-poor) peri-
 187 dotite samples, hereafter referred to as Primitive Synthetic Upper Mantle (PSUM) and
 188 Depleted Synthetic Upper Mantle (DSUM, Figure 2b), respectively. The mixing line ap-
 189 proximates the widest array of mantle compositions derived from the natural rock record
 190 and may be interpreted as representing the first order composition variation in response
 191 to melt extraction (depletion) or addition (refertilization) in the mantle. The mixing line
 192 therefore provides a basis for sampling synthetic bulk mantle compositions directly from
 193 PC space, which were then used to generate RocMLM training data.

Table 1: Summary of the filtered and standardized peridotite dataset from Earth-chem.org. Columns with an asterisk are in wt.%. Std = standard deviation, IQR = interquartile range.

Oxide	Measured	Missing	Min*	Max*	Mean*	Median*	Std*	IQR*
SiO ₂	3111	0	36.7	52	44.1	44.1	1.16	1.24
TiO ₂	2835	276	0	0.268	0.051	0.03	0.05	0.068
Al ₂ O ₃	3111	0	0.023	4.95	1.65	1.31	1.14	1.82
FeOT	3111	0	5.98	15.3	8.05	8.01	0.675	0.569
MgO	3111	0	31.8	50.8	43	43.6	2.96	4.38
CaO	3111	0	0.01	5.2	1.46	1.17	1.04	1.66
Na ₂ O	2008	1103	0	0.525	0.127	0.098	0.11	0.171

194 **2.1.3 Reducing Bulk Mantle Compositions to a Single Fertility Index
 195 Value**

196 Training RocMLMs with either 7 oxide components or two PCs as inputs is pos-
 197 sible. However, our targeted application (e.g., implementing RocMLMs in geodynamic
 198 codes) discourages the use of the two options because in either case it would require track-

199 ing the oxides in numerical geodynamic codes, which is currently impractical. Thus, we
 200 aimed to reduce the dimensionality of the training dataset from nine dimensions (7 ox-
 201 ide components + PT) to three dimensions (1 compositional dimension + PT) by es-
 202 timating the amount of melt extraction (depletion) that might have produced the syn-
 203 synthetic bulk mantle compositions in the training dataset. Assuming that all synthetic sam-
 204 ples were derived from a PSUM source, we adopt a simple modal fractional melting model
 205 (after Shaw, 1970):

$$\frac{C_{\text{TiO}_2}^s}{C_{\text{TiO}_2}^0} = R = (1 - F)^{\frac{1}{D_0} - 1} \quad (2)$$

206 where R is the ratio of the TiO_2 concentration of the sample to the initial PSUM source
 207 (Table 2), F is the melt fraction, and $D_0 = 0.05$ is the bulk distribution coefficient for
 208 TiO_2 in peridotite (after Brown and Lesher, 2016). Note that unlike the dataset of nat-
 209 ural peridotite samples, synthetic samples were drawn directly from PC space and their
 210 TiO_2 concentrations (and other oxide components) change monotonically with PC1 from
 211 the initial PSUM source (Figure 2b,c). Synthetic samples therefore represent a smooth
 212 and idealized variability from fertile (PSUM) to depleted (DSUM) mantle compositions
 213 that captures the average variation in natural peridotite samples.

214 A Fertility Index (ξ) is calculated by rearranging Equation (2) for F and subtract-
 215 ing F from 1:

$$\xi = 1 - F = R^{\frac{1}{(D_0)^{-1}}} \quad (3)$$

216 Training RocMLMs on ξ instead of seven oxide components is beneficial for two
 217 reasons: 1) it greatly increases RocMLM efficiency and 2) unlike oxide components or
 218 PCs, melt fraction is routinely implemented in numerical geodynamic simulations (e.g.,
 219 Cerpa et al., 2019; Gerya and Yuen, 2003; Kelley et al., 2010; Li et al., 2019; Sizova et al.,
 220 2010; Yang and Faccenda, 2020). Likewise, tracking the depletion/fertility of the man-
 221 tle in geodynamics models with Lagrangian tracers and/or compositional fields is more
 222 conceivable (Agrusta et al., 2015; Cagnioncle et al., 2007; Gerya and Meilick, 2011; Tack-
 223 ley and Xie, 2003). Although we chose ξ for RocMLM training, ξ and F represent op-
 224 posite reference frames for the same time-integrated melting process, and are therefore

225 interchangeable. This approach offers a generalized solution for coupling RocMLMs to
 226 geodynamic codes.

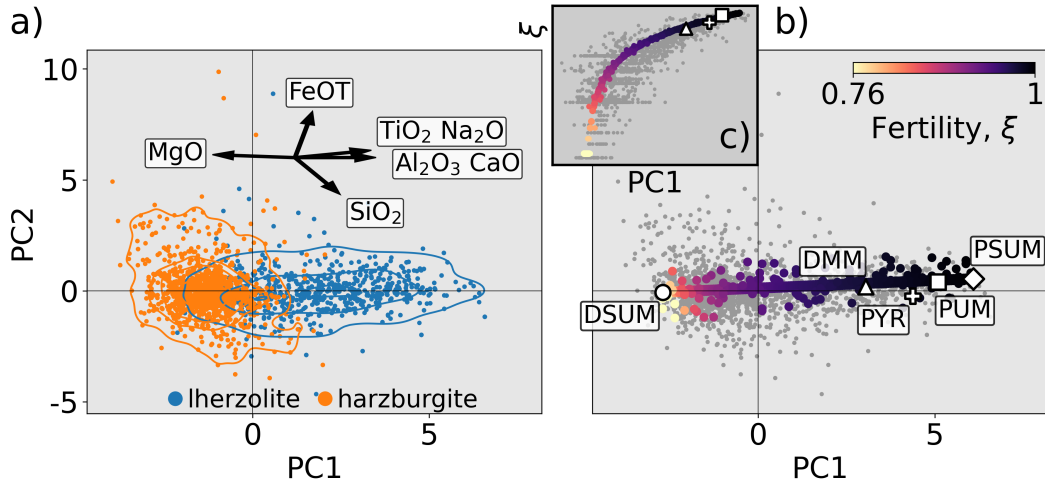


Figure 2: PC1-PC2 diagrams showing the standardized geochemical dataset of natural peridotite samples (a) and a mixing array between hypothetical end-member mantle compositions Primitive Synthetic Upper Mantle (PSUM) and Depleted Synthetic Upper Mantle (DSUM, b). Black arrows in (a) indicate PCA loading vectors. Colored data points in (b) are the synthetic mantle compositions used to train RocMLMs, which were sampled independently from the natural peridotite samples (gray data points). The inset (c) shows how the Fertility Index (ξ) changes nonlinearly with PC1. DMM, PUM, and PYR are from Table 2.

227 The melting model in Equation (2) is oversimplified since it assumes: 1) melt is in-
 228stantaneously removed from the source region, 2) D_0 is constant, and 3) minerals melt
 229 in the same proportions that they exist in the source rock. It nevertheless provides an
 230 efficient parameterization of the variation in mantle composition as a function of melt
 231 extraction and addition. Equation (2) predicts that a Depleted MORB Mantle (DMM)
 232 composition is produced through a time-integrated 2.2% melt extraction from a Prim-
 233 itive Upper Mantle (PUM) source (Table 2). This result is consistent with the degree
 234 of depletion inferred from trace element patterns and mass balance constraints (2-3%
 235 melt removal from PUM, Workman and Hart, 2005). We therefore consider ξ an ade-
 236 quate first-order proxy for describing the variations in bulk mantle composition used in
 237 our RocMLM training dataset. However, given that TiO₂ concentrations are strongly
 238 affected by reactive melt transport (e.g., Le Roux et al., 2007), ξ may only be estimated
 239 for the average compositional trend as expressed in PC1-PC2 space, rather than on in-
 240 dividual peridotite samples.

Table 2: Hypothetical upper mantle end-member compositions. Columns with an asterisk are in wt.%. Depleted MORB Mantle (DMM) is from Workman and Hart (2005), Primitive Upper Mantle (PUM) is from Sun and McDonough (1989), and Pyrolite (PYR) is from Green (1979). Primitive Synthetic Upper Mantle (PSUM) and Depleted Synthetic Upper Mantle (DSUM), are end-member compositions derived in this study.

Sample	SiO_2^*	TiO_2^*	Al_2O_3^*	FeOT^*	MgO^*	CaO^*	Na_2O^*	ξ
DSUM	44.1	0.0012	0.261	7.96	47.4	0.22	0.042	0.764
DMM	44.7	0.13	3.98	8.18	38.7	3.17	0.13	0.974
PYR	45	0.16	4.4	7.6	38.8	3.4	0.34	0.984
PUM	44.9	0.2	4.44	8.03	37.7	3.54	0.36	0.996
PSUM	46.2	0.216	4.88	8.88	35.2	4.34	0.33	1

241 2.2 Generating RocMLM Training Data

242 We used the GFEM program Perple_X (version 7.0.9, Connolly, 2009) to generate
 243 RocMLM training data across PT conditions as described in Section 2.1.1 and synthetic
 244 bulk mantle compositions as described in Section 2.1.2. The Perple_X calculations were
 245 constrained to the $\text{Na}_2\text{O}-\text{CaO}-\text{FeO}-\text{MgO}-\text{Al}_2\text{O}_3-\text{SiO}_2$ (NCFMAS) chemical system to com-
 246 ply with the thermodynamic data and solution models of Stixrude and Lithgow-Bertelloni
 247 (2022). The Stixrude and Lithgow-Bertelloni (2022) dataset (stx21ver.dat) was used be-
 248 cause our initial tests with alternative thermodynamic datasets (hp02ver.dat and hp633ver.dat,
 249 Connolly and Kerrick, 2002; Holland et al., 2018; Holland and Powell, 2001) failed to re-
 250 produce the seismic wave velocities of geophysical reference models (PREM and STW105,
 251 Dziewoński and Anderson, 1981; Kustowski et al., 2008) with sufficient accuracy because
 252 these datasets lack a parametrization of the shear modulii of the minerals phases. Note
 253 that our Perple_X calculations ignored TiO_2 , which was initially included to define ξ and
 254 derive synthetic bulk mantle compositions. Despite being measured as a major oxide com-
 255 ponent, the average TiO_2 content of our standardized samples is 0.05 ± 0.1 wt.% (2σ ,
 256 Table 1). Such small concentrations of TiO_2 may safely be ignored in phase relation cal-
 257 culations with negligible effects on the RocMLM training dataset.

258 The Perple_X models used to generate the present RocMLM training database in-
 259 cluded equations of state for solution phases: olivine, plagioclase, spinel, clinopyroxene,

wadsleyite, ringwoodite, perovskite, ferropericlase, high-pressure C2/c pyroxene, orthopyroxene, akimotoite, post-perovskite, Ca-ferrite, garnet, and Na-Al phase. Melt was not considered due to the absence of melt models in the Stixrude and Lithgow-Bertelloni (2022) dataset, but may be considered in future versions of training datasets if the elastic parameters in hp02ver.dat are corrected. Once configured, Perple_X generated RocMLM training data (density, as well as P- and S-wave seismic velocities) by minimizing the total Gibbs Free Energy of a multicomponent multiphase thermodynamic system at fixed PTX conditions (Gibbs, 1878; Spear, 1993). The reader is referred to Connolly (2009) and Riel et al. (2022) for a complete description of the GFEM problem.

In principle, applying identical sets of solution phase models, thermodynamic data, and bulk compositions will define identical Gibbs Free Energy hyperplanes. This implies that any GFEM algorithm should converge on identical phase relations. Thus, although this study uses Perple_X exclusively, an identical set of training data can be generated by applying the procedures outlined above to other GFEM programs. Note that RocMLM capabilities and performance are primarily dependent on the size and the range of PTX conditions of the training dataset, not on the choice of GFEM algorithm.

2.3 Training RocMLMs

RocMLM training data were preprocessed using the following procedure. First, two-dimensional grids of rock properties (“pseudosections”) calculated by Perple_X were stacked into a three-dimensional array, $Z = (z_{1,1,1}, \dots, z_{n,w,w})$, where $w = 128$ is the resolution of the PT grid and $n = 128$ is the number of random synthetic bulk mantle compositions represented by a ξ value. Z was flattened into arrays of training features (PT and ξ), $X = (x_{1,1,1}, \dots, x_{v,v,v})$, and training targets (density, Vp, and Vs), $y = (y_{1,1,1}, \dots, y_{v,v,v})$, where $v = n \cdot w^2 = 128^3$ is the total number of training examples. Following common practice, X and y were scaled using “z-score normalization” before training.

The preprocessed training data were then fit with three different nonlinear regression algorithms (Decision Tree: DT, k-Neighbors: KN, and Neural Networks: NN) from the scikit-learn python library (Pedregosa et al., 2011). Each regression algorithm was tuned with a grid search approach, where a performance score (RMSE) was evaluated over all hyperparameter combinations relevant to the particular regression algorithm (Ta-

ble 3). The set of hyperparameters that produced the best score (lowest RMSE) was used to train the RocMLM.

Table 3: RocMLM configuration. Hyperparameter values in parentheses are tested sequentially by a cross-validation grid search algorithm and the best set of hyperparameters is chosen by the lowest RMSE. Hyperparameters that are not shown use default values (see regression model documentation on scikit-learn.org).

Model	Hyperparameter	Value	Tuned
DT	splitter	(best, random)	tuned
	max features	(1, 2, 3)	tuned
	min samples leaf	(1, 2, 3)	tuned
	min samples split	(2, 4, 6)	tuned
KN	n neighbors	(2, 4, 8)	tuned
	weights	(uniform, distance)	tuned
NN1	hidden layer sizes	(8, 16, 32)	tuned
NN2	hidden layer sizes	([16, 16], [32, 16], [32, 32])	tuned
NN3	hidden layer sizes	([32, 16, 16], [32, 32, 16], [32, 32, 32])	tuned
NN(all)	learning rate	(0.001, 0.005, 0.001)	tuned
	batch size	20%	fixed
	max epochs	100	fixed

2.4 Evaluating RocMLM Accuracy and Performance

Connolly and Khan (2016) estimated the uncertainties of Vp and Vs to be on the order of 3–5% within the same thermodynamic framework used to generate RocMLM training data (Stixrude and Lithgow-Bertelloni, 2005). We can therefore consider the base-uncertainty of RocMLM predictions to be 3–5%. RocMLM predictions must also account for additional uncertainties that are introduced during RocMLM training (i.e., the variance of residuals between RocMLM predictions and targets), which are about 2% for NN1 and < 1% for DT, KN, and NN3. Assuming the lowest-uncertainty models (DT, KN, NN3) would be preferred for geodynamic applications, we ignore the small variances introduced during training (< 1%) and evaluate the total RocMLM prediction uncertain-

ties to be on the same order as the base GFEM uncertainty (3–5%) after Connolly and Khan (2016).

RocMLM accuracy (in terms of RMSE) was evaluated by: 1) testing RocMLMs on a separate validation dataset to determine the generalization capacity of RocMLMs to unseen mantle conditions (internal accuracy), and 2) comparing RocMLMs predictions with geophysical reference models PREM and STW105 (external accuracy). The first test evaluates the degree to which RocMLMs can reproduce GFEM predictions. The second test evaluates the degree to which the “true data” used for RocMLM training reproduces the phase transitions actually observed in Earth’s upper mantle, which depend on the thermodynamic data, GFEM algorithm, and parameterization used to describe the composition of mantle rocks (i.e., ξ).

The validation dataset was generated by Perple_X in the same manner as the training dataset, but shifted by one-half step (in the positive PT directions) so that RocMLM predictions could be evaluated at completely independent PT conditions. RocMLM performance was evaluated by: 1) measuring single-point prediction times (execution speed), and 2) scaling execution speed by RocMLM file size (disk space) to account for information compression (model efficiency).

The number of PT points and synthetic bulk mantle compositions used for generating training data were varied from 8 to 128 (2^{11} – 2^{21} total training examples) to test the sensitivity of RocMLM accuracy and performance with respect to the size (“capacity”) and composition of the training dataset. The same sets of training data were also used to evaluate single-point execution speed using a common Lookup Table approach, where a cubic spline interpolation was applied to the training dataset and rock properties were evaluated at arbitrary PTX conditions. Prediction accuracy and performance were measured in a consistent manner so that direct comparisons could be made between RocMLMs, Lookup Tables, and GFEM programs.

3 Results

3.1 RocMLM Accuracy

The following examples of Decision Tree (DT, Figure 3), single-layer Neural Network (NN1, Figure 4), and three-layer Neural Network (NN3, Figure 5) models demon-

332 strate how different regression algorithms ultimately influence the accuracy of RocMLM
 333 predictions (see Supplementary Information for all regression algorithms).

334 DT predictions are practically indistinguishable from that of Perple_X, indicating
 335 a nearly-perfect mapping of the validation dataset by the DT algorithm (RMSE for den-
 336 sity: 0.01 g/cm³, Vp and Vs: 0.02 km/s, Figure 3). Absolute differences between Per-
 337 ple_X and DT predictions (residuals) are broadly dispersed and approach zero in most
 338 regions of PT space. Some concentrations of residuals exist near phase transitions, but
 339 are subtle and discontinuous (Figure 3g–i).

340 In contrast, NN1 predictions are notably smoother than Perple_X (Figure 4), with
 341 higher errors (RMSE for density: 0.02 g/cm³, Vp: 0.06 km/s, Vs: 0.05 km/s) that in-
 342 dicate an inability to resolve sharp gradients in physical properties when using a single-
 343 layer Neural Network with a small to moderate amount of neurons. This is evident by
 344 the NN1 residuals, which are systematically concentrated near phase transitions (Fig-
 345 ure 4g–i). NN1 profiles display relatively weak discontinuities with gradual changes in
 346 physical properties across the olivine → wadsleyite and ringwoodite → bridgmanite +
 347 ferropericlase transitions (Figure 4j–l), and phase transformations within the MTZ are
 348 virtually absent compared to DT and NN3 profiles. While NN1 predictions do not re-
 349 produce the validation dataset or geophysical profiles with the highest accuracy, deeper
 350 (and/or wider) NN architectures with more hidden-layers (e.g., NN3) are more capable
 351 (Figure 5). NN3 predictions fit the validation dataset and resolve discontinuities in geo-
 352 physical profiles with nearly equivalent accuracy as DT and KN algorithms (compare
 353 profiles in Supplementary Information).

354 Comparing density, Vp, and Vs depth profiles predicted by RocMLMs (for an av-
 355 erage mid-ocean ridge-like geotherm with a mantle potential temperature of 1573 K) with
 356 PREM and STW105 reveals relatively low errors (density: ≤ 0.08 g/cm³, Vp: ≤ 0.26
 357 km/s, Vs: ≤ 0.14 km/s) and high correlations ($R^2 \geq 0.94$) that indicate good agreement
 358 between seismically-derived profiles and thermodynamic predictions, irrespective of re-
 359 gression algorithm (compare profiles in the Supplementary Information). The largest de-
 360 viations between RocMLM profiles, PREM, and STW105 fall within two regions: 1) be-
 361 tween 1–8 GPa, and 2) at the base of the MTZ (Figures 3–5j–l). At pressures lower than
 362 5 GPa, the divergence between RocMLM profiles and seismically-derived profiles may
 363 be explained by the low resolution of the 1D geophysical profiles relative to the extreme

364 spatial variability in composition and geotherms on Earth. Tests using an average con-
 365 tinental geotherm to calculate RocMLM profiles results in less divergence between RocMLM
 366 profiles and PREM at < 5 GPa compared to the mid-ocean ridge-like geotherms used
 367 to build the profiles presented in Figures 3–5. At pressures between 5–8 GPa, the two
 368 geophysical models show a discrepancy: PREM contains a discontinuity, especially in
 369 seismic velocities, while STW105 has a gradual and continuous increase. RocMLM pro-
 370 files between 5–8 GPa are more similar to STW105, which does not map any disconti-
 371 nuous until the olivine → wadsleyite transition at 410 km depth (Figures 3–5j–l).

372 Within the MTZ, DT and NN3 profiles predict intermediate discontinuities, while
 373 PREM and STW105 are gradual and continuous (Figures 3,5g–i). As expected, compar-
 374 ing RocMLM profiles for different geotherms shows that the choice of a mantle poten-
 375 tial temperature leads to contrasting predictions of: 1) the overall evolution of rock prop-
 376 erties with depth, and 2) the depths, magnitudes, and sharpness of phase transitions within
 377 the MTZ (Figures 3–5g–i). RocMLM profiles show, similarly to those directly derived
 378 from the Perple_X calculation, temperature-sensitive discontinuities at the olivine → wad-
 379 sleyite and wadsleyite → ringwoodite transitions, but a rather temperature insensitive
 380 ringwoodite → bridgemanite + ferropericlase transition (Figures 3–5g–i). This can be ex-
 381 plained by differences in Clapeyron slopes modeled by the Stixrude and Lithgow-Bertelloni
 382 (2022) dataset.

383 3.2 RocMLM Performance

384 We now compare RocMLM performance to two other tools classically used to pre-
 385 dict the variations of physical properties of mantle rocks in geodynamic models: GFEM
 386 programs and Lookup Tables. Note that RocMLM, GFEM, and Lookup Table perfor-
 387 mance is platform specific. Running analogous implementations with other programming
 388 languages and/or on alternative computer hardware will differ from the results presented
 389 here. All computations in this study were made using CPUs of a Macbook Pro (2022;
 390 M2 chip) with macOS 13.4 and using Python 3.11.4. All performance metrics were eval-
 391 uated with a single CPU core.

392 Figure 6 shows how execution speed, efficiency, and accuracy scale with the capac-
 393 ity of Lookup Tables and RocMLMs. Here, “capacity” refers to the number of scalar val-
 394 ues stored by Lookup Tables, or alternatively, the number of pseudosection PTX points

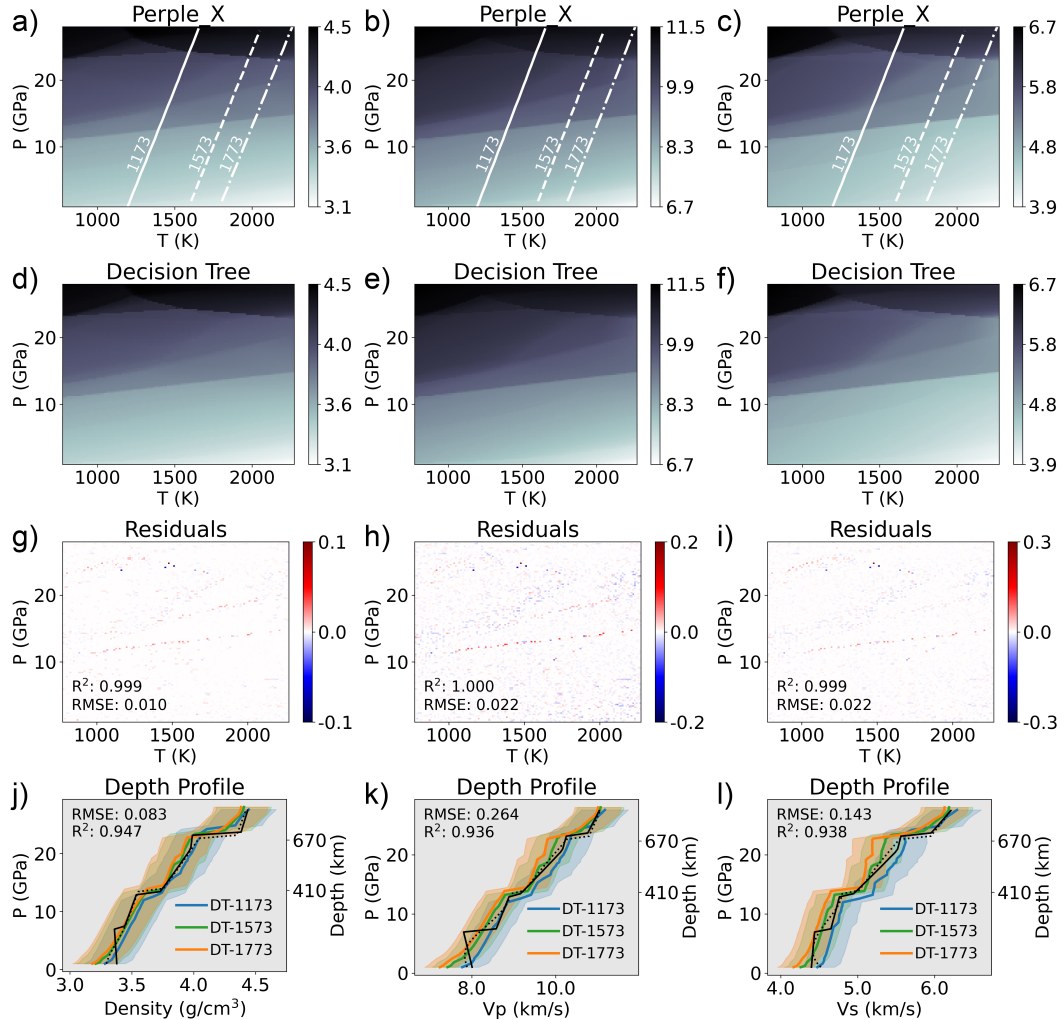


Figure 3: PT diagrams showing density (left column, g/cm^3), V_p (middle column, km/s), and V_s (right column, km/s) predictions from a Perple_X model with a PUM bulk composition (a–c), a Decision Tree RocMLM (d–f), and absolute differences between Perple_X and DT (g–i) measured on the validation dataset. Depth profiles (j–l) compare Perple_X and DT predictions extracted along a $0.5 \text{ K}/\text{km}$ adiabat with different mantle potential temperatures (white lines) with reference models PREM (solid black line, Dziewoński and Anderson, 1981) and STW105 (dotted black line, Kustowski et al., 2008). The RMSE in (j–l) indicates the measured differences between DT-1573 and PREM. Colored ribbons indicate 5% uncertainty in RocMLM predictions.

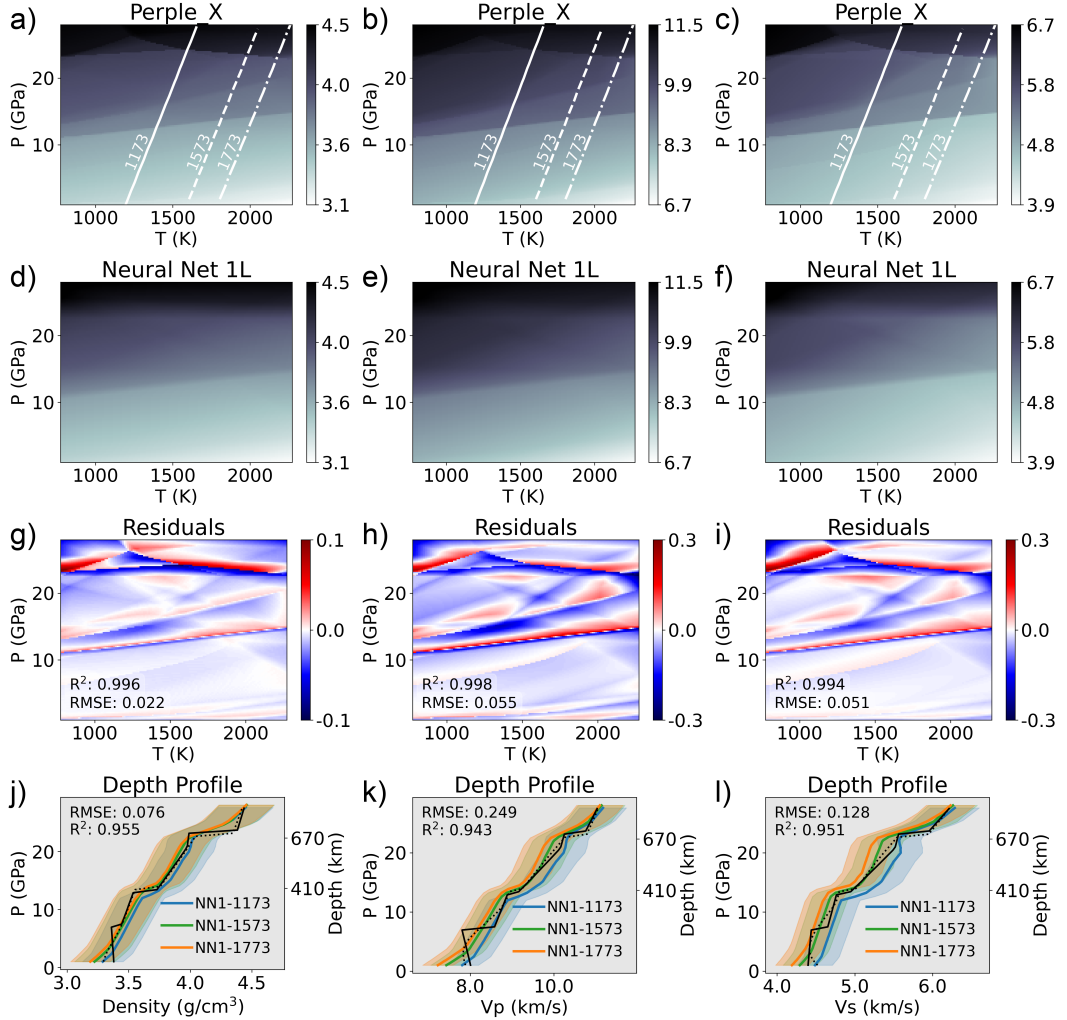


Figure 4: PT diagrams showing density (left column, g/cm^3), V_p (middle column, km/s), and V_s (right column, km/s) predictions from a Perple_X model with a PUM bulk composition (a–c), a single-layer Neural Network RocMLM (d–f), and absolute differences between Perple_X and NN1 (g–i) measured on the validation dataset. Other legend details are the same as in Figure 3.

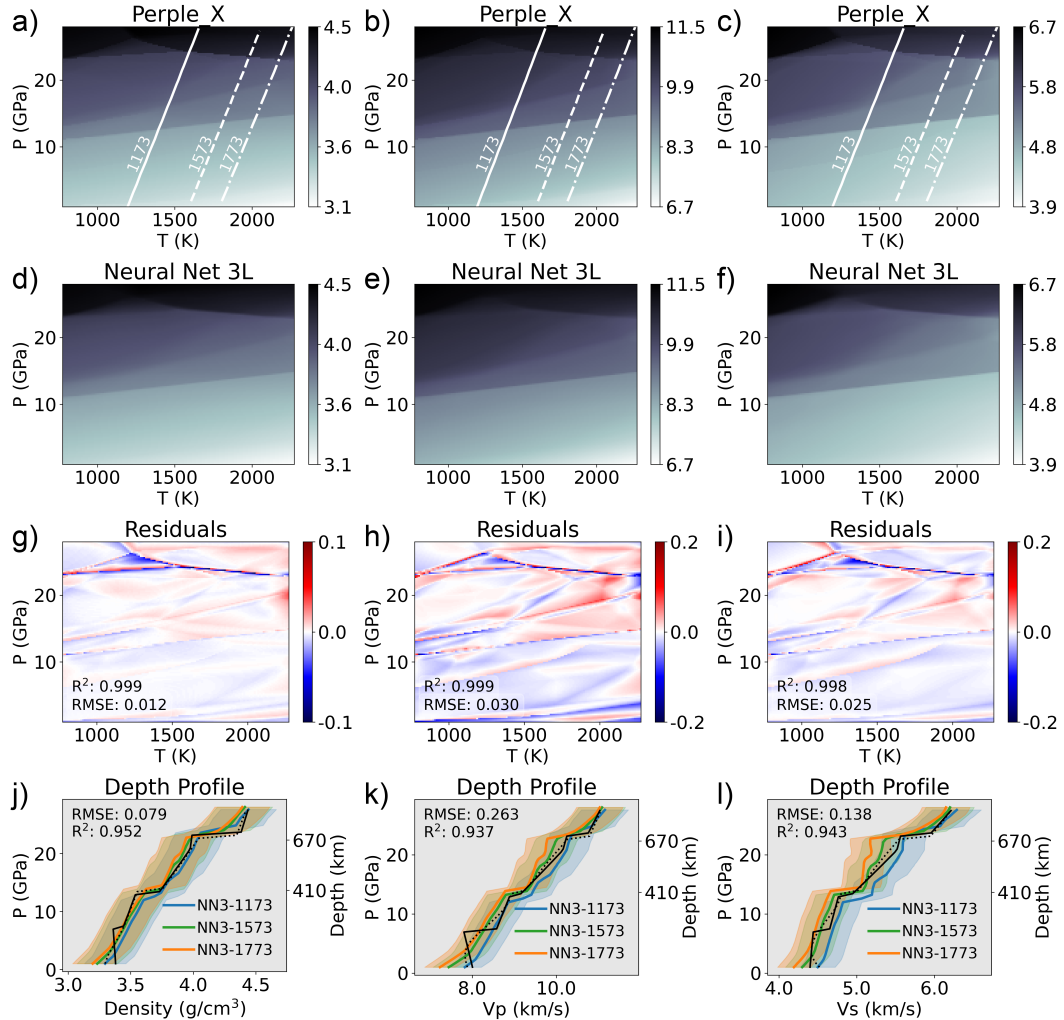


Figure 5: PT diagrams showing density (left column, g/cm^3), V_p (middle column, km/s), and V_s (right column, km/s) predictions from a Perple_X model with a PUM bulk composition (a–c), a three-layer Neural Network RocMLM (d–f), and absolute differences between Perple_X and NN3 (g–i) measured on the validation dataset. Other legend details are the same as in Figure 3.

“learned” by RocMLMs. Thus, “capacity” is intended to convey and compare the breadth of petrological “knowledge”, or predictive capabilities, of Lookup Tables and RocMLMs. Within the same context, the notion of “capacity” is irrelevant for GFEM programs. Rather, GFEM performance primarily scales with the number of chemical components, phase solutions, and size of the compositional space defined by the user, as well as automatic grid refinement settings and other user-defined configuration options.

GFEM performance is reported using the range of average execution speeds (4–228 ms) and efficiencies (60–3138 ms·Mb) that we measured while generating our RocMLM training datasets as described in Section 2.2. To demonstrate the sensitivity of GFEM performance to alternative Perple_X configurations, we also show GFEM execution speed and efficiency for similar calculations using the thermodynamic data and phase solutions of Holland et al. (2018). Note that none of the Perple_X calculations using the Holland et al. (2018) configuration were used to train RocMLMs due to inaccurate seismic velocity predictions, and their performance metrics are only shown for illustrative purposes.

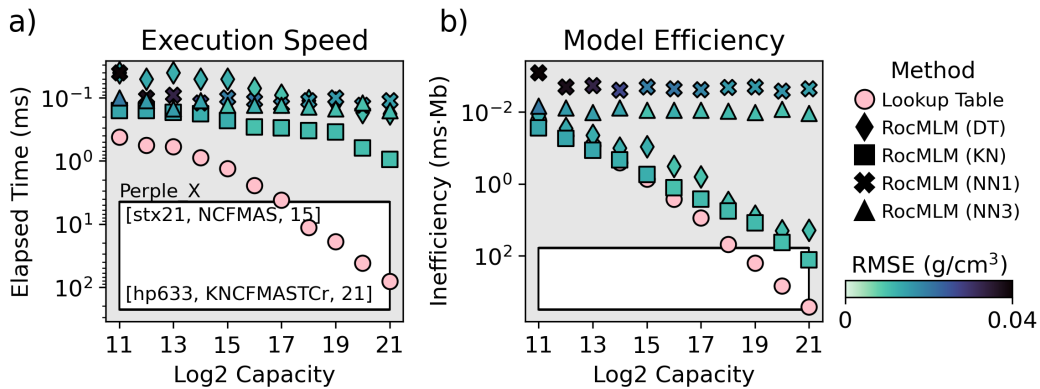


Figure 6: Computational efficiency of various approaches in terms of execution speed (a) and model efficiency (b). “Capacity” (x-axis) is a proxy for the petrological “knowledge”, or predictive capabilities, of Lookup Tables and RocMLMs. White regions indicate GFEM efficiencies for different Perple_X configurations (thermodynamic dataset, chemical system, and number of solution phases are indicated in square brackets). stx21: Stixrude and Lithgow-Bertelloni (2022), hp633: Holland and Powell (2011) updated in Holland et al. (2018). Perple_X was run without multilevel grid refinement. RMSE is measured between density predictions and the validation dataset.

For Lookup Tables, execution speed and efficiency both scale roughly linearly with capacity on a logarithmic scale—indicating an inverse power-law relationship between Lookup Table capacity and performance (Figure 6). RocMLM performance, in contrast,

scales differently depending on the performance metric and regression algorithm. For example, RocMLM execution speed remains roughly constant, or increasing slightly with capacity, and shows relatively small variance among all regression algorithms (0.14 ± 0.26 ms, 2σ , Figure 6a). Yet RocMLM efficiency is markedly different for DT and KN algorithms compared to NN algorithms (Figure 6b). Despite the fast execution times of KN and DT algorithms (Figure 6a), their efficiency scales roughly linearly with capacity on a logarithmic scale—indicating an inverse power-law relationship between efficiency and capacity similar to Lookup Tables (Figure 6b). NN algorithms, on the other hand, show roughly constant efficiencies that indicate a high degree of information compression without sacrificing execution speed (Figure 6b). We note that training times for NN algorithms are many orders of magnitude larger than DT and KN algorithms (Supplementary Information). However, training times are neither limiting nor critical for geodynamic applications as training is independent from, and precedes numerical simulations.

Since accuracy is measured relative to the rock properties generated by GFEM programs, GFEM programs have perfect accuracy by definition. With respect to RocMLMs, validation accuracies (RMSE) are observed to be roughly constant for regression algorithms that apply binary decisions or local distance-based weights (DT and KN), while algorithms that apply global activation-based weights (NNs) show a positive correlation between accuracy and capacity (Figure 6). In addition to improving accuracy with increasing amounts of training examples, NN accuracy also increases with the number of hidden-layers (Figure 6) because deeper networks are more capable of fitting sharp gradients in the training data (see Supplementary Information for examples of NN1, NN2, and NN3 RocMLMs). We also tested the effects of NN width (changing the number of nodes within each hidden layer), but this had a negligible impact on NN performance and accuracy compared to increasing NN depth.

4 Discussion

4.1 RocMLM Performance Tradeoffs

RocMLM performance and accuracy are both critical for geodynamic applications and crucial for determining if RocMLMs are an improvement over methods commonly used for predicting rock properties in numerical geodynamic simulations. In terms of pure execution speed, our testing demonstrates that RocMLMs can make predictions between

443 10^1 – 10^3 times faster than GFEM programs and Lookup Tables (Figure 6), depending
444 on the GFEM program configuration. The difference in execution speed between Lookup
445 Tables and RocMLMs is small for low-resolution models (Figure 6) that are limited to
446 ≤ 16 mantle compositions and large PT intervals (≥ 1.7 GPa and 100 K PT step sizes).
447 However, such low-resolution models are not an obvious improvement over simple poly-
448 nomial approximations of a selective number of important phase transformations. At higher
449 resolutions, RocMLMs can accurately resolve the physical properties of all thermodynamically-
450 stable mineral assemblages in fine detail (at PT intervals of ≤ 0.2 GPa and 12 K) and
451 for a wide variety of bulk mantle compositions (Figure 2). In addition to their broad pre-
452 dictive capabilities, high-resolution RocMLMs make predictions at speeds (approximately
453 0.1–1 ms, Figure 6) that allow computation of physical properties at the node-scale dur-
454 ing geodynamic simulations. We therefore argue that high-resolution RocMLMs over-
455 come all practical limitations for implementing thermodynamically self-consistent den-
456 sity evolution in numerical geodynamic models.

457 With respect to ranking the practicality of different RocMLM for geodynamic ap-
458 plications, execution speeds and accuracies alone suggest that high-resolution RocMLMs
459 will perform with roughly equivalent outcomes regardless of the regression algorithm (Fig-
460 ure 6a). However, our testing reveals an obvious tradeoff between RocMLM performance
461 and accuracy when accounting for compression ratio (i.e., the amount of “learned” in-
462 formation relative to the RocMLM file size). Figure 6b shows DT and KN algorithms
463 becoming rapidly inefficient compared to NNs as the capacity of the training dataset in-
464 creases. This is because NN algorithms require relatively little information to make pre-
465 dictions after training (weights and biases for each neuron) compared to DT (tree struc-
466 ture: nodes, splits, and predictions) and KN (entire training dataset with distance weights)
467 algorithms. Moreover, accuracy tends to improve monotonically with dataset capacity
468 for NN, but not for DT or KN. We therefore argue that deep NN RocMLMs are the most
469 practical choice for geodynamic applications for three reasons: 1) modeling more rock
470 types only requires adding more training data, 2) adding more training data improves
471 prediction accuracy without diminishing performance, and 3) further improvements and
472 adaptations to different geodynamic applications are possible by exploring different ar-
473 chitectures than the simple NN models we have tested thus far.

474 The main limitations of NN RocMLMs are twofold: 1) training is computationally
475 expensive compared to other regression algorithms (Supplementary Information) and 2)

shallow NN architectures imply smoother gradients in rock properties than GFEM calculations. We do not consider these limitations critical because training time is independent from RocMLM performance and even if deeper NN architectures are needed to fit discontinuities in rock properties with high accuracy, the number of layers and neurons in each layer remains small (Table 3). We note that our testing has been limited to the prediction of three properties that are mostly P-dependent and are relatively continuous despite a few large discontinuities. In principle, RocMLMs can be trained on any thermodynamic variable output by GFEM programs. However, we have not yet trained RocMLMs on more discrete, discontinuous, and/or highly T-dependent variables, such as modal proportions of minerals, volatile contents, or melt fraction, which will be treated in future developments of RocMLMs.

487 4.2 Geophysical and Thermodynamic Estimates of Elastic Properties

488 The amount of overlap between RocMLM profiles and PREM (Figures 3–3) suggests
 489 good agreement between thermodynamic and geophysical estimates of the elastic
 490 properties of mantle rocks within the limits of our training dataset and Perple_X config-
 491 uration (see Sections 2.1 and 2.2). Discrepancies between thermodynamic profiles and
 492 PREM can be explained by chemical heterogeneity and/or differences in mantle geotherms
 493 that modify phase relations (Goes et al., 2022; Karki and Stixrude, 1999; Karki et al.,
 494 2001; Stixrude and Lithgow-Bertelloni, 2012; Waszek et al., 2021; Xu et al., 2008). Be-
 495 cause the RocMLM training dataset spans a wide array of synthetic bulk mantle com-
 496 positions, we can directly test the sensitivity of thermodynamic estimates to changes in
 497 bulk FeO–MgO contents (Figure 7).

498 As Fertility Index (ξ) increases by refertilization and/or lack of melt extraction and
 499 the bulk mantle composition becomes more Fe-rich (and more dense), Vp and Vs respond
 500 (both positively and negatively) according to the equations of state described in Stixrude
 501 and Lithgow-Bertelloni (2005). RocMLM training data show that density is the least sen-
 502 sitive parameter to ξ overall with only modest variations across a broad range of man-
 503 tle rocks from fertile to highly depleted ($\xi = 0.76$, Figure 7a). The largest density vari-
 504 ations occur at pressures below the olivine → wadsleyite transition (< 410 km), yet are
 505 still small enough (approximately 3–5 %) to imply that spontaneous mantle convection
 506 requires strong thermal gradients and/or hydration by metamorphic fluids in addition
 507 to melt extraction.

508 In contrast to density, Vp and Vs are more sensitive to ξ overall, especially at pres-
 509 sures above the olivine \rightarrow wadsleyite transition (> 410 km). RocMLM training data sug-
 510 gests that an “optimal” Vp/Vs profile requires a more depleted mantle between 410–670
 511 km and a more fertile mantle at < 410 km (Figure 7b,c). Forming this compositional
 512 layering pattern is counterintuitive, however, as partial melting is expected to be more
 513 pervasive at lower pressures. Moreover, density profiles are incongruent with this pat-
 514 tern, suggesting instead that a depleted mantle at < 410 km and more fertile mantle at
 515 > 410 km are required for an optimal fit with PREM and STW105 (Figure 7a).

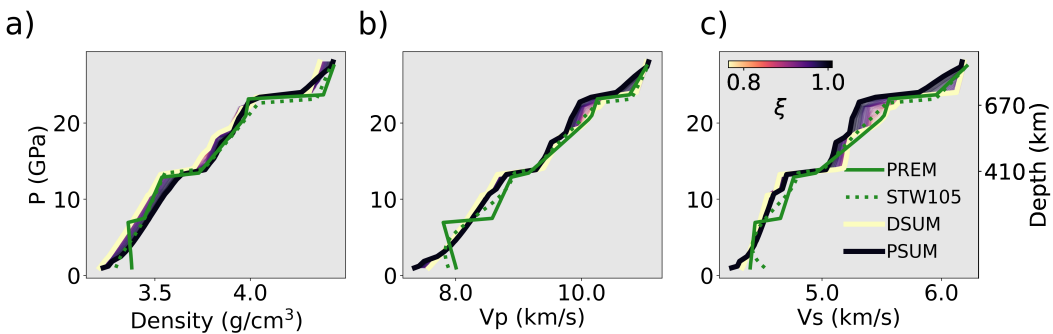


Figure 7: Depth profiles of RocMLM training data along a 1573 K mantle adiabat showing the sensitivities of thermodynamic estimates of density (a), Vp (b), and Vs (c) to changes in bulk mantle composition (as represented by the Fertility Index, ξ). Geo-physical profiles PREM and STW105 (green lines) and the profiles of synthetic mantle end-member compositions PSUM and DSUM (thick colored lines) are shown for reference. Thin colored lines show profiles for the entire range of RocMLM training data.

5 Conclusions

The dynamics of Earth’s upper mantle is largely driven by density contrasts stemming from changes in PT conditions, which lead to phase transformations in mantle rocks. These phase transformations also modify the elastic properties of mantle rocks. Therefore phase changes must be considered when inverting present-day mantle structure from seismic data. Likewise, numerical geodynamic simulations of mantle convection must account for thermodynamics, but are typically implemented with simple PT-dependent parameterizations of rock properties and phase boundaries that do not explicitly account for changes in Gibbs Free Energy resulting from changes in PT and in bulk composition. Here, we introduce RocMLMs as an alternative to GFEM programs and we evaluate RocMLM performance and accuracy. We also show how the RocMLM predictions compare to PREM and STW105. Our main findings are as follows:

- 528 1. RocMLMs predict density and elastic properties with high accuracy and are up
 529 to 101–103 faster than commonly used methods. This improvement in prediction
 530 speed makes thermodynamically self-consistent mantle convection within high-resolution
 531 numerical geodynamic models practical for the first time.
- 532 2. RocMLMs trained with moderately deep (3 hidden layers) NNs are more robust
 533 and efficient compared to RocMLMs trained with other regression algorithms, and
 534 are therefore the most practical models for coupling with numerical geodynamic
 535 codes.
- 536 3. RocMLM training data are sensitive to bulk mantle composition and geothermal
 537 gradients, yet show good agreement with PREM and STW105 for an average man-
 538 tle geotherm.

539 Based on our results, we argue that moderately deep NN RocMLMs can be excep-
 540 tional emulators of GFEM programs in geodynamic simulations that require computa-
 541 tionally efficient predictions of rock properties. We have demonstrated that RocMLMs
 542 perform remarkably well for dry mantle rocks with compositions ranging from very fer-
 543 tile lherzolites to strongly depleted harzburgites and PT conditions ranging from 1–28
 544 GPa and 773–2273 K.

545 Moreover, the RocMLM approach can be used with any GFEM program and ther-
 546 modynamic dataset. Any improvement to the underlying thermodynamic data should
 547 further increase the accuracy of RocMLM predictions. Testing RocMLMs predictions
 548 on other thermodynamic variables of interest, including modal proportions of minerals,
 549 volatile contents, and melt fractions will be the focus of future studies. Likewise, in fu-
 550 ture works, we will extend the training data to include hydrous systems and additional
 551 end-member mantle compositions (e.g., pyroxenites and dunites).

552 6 Acknowledgements

553 This work was supported by the Tremplin-ERC grant LEARNING awarded to Nestor
 554 Cerpa by the I-SITE excellence program at the Université de Montpellier. We thank Mau-
 555 rine Montagnat, Fernando Carazo, Nicolas Berlie, and many researchers and students
 556 at Géosciences Montpellier for their thoughtful feedback during the development of this
 557 work. We gratefully acknowledge additional support from the European Research Coun-

558 cil (ERC) under the European Union Horizon 2020 Research and Innovation program
559 grant agreement No. 882450 (ERC RhEoVOLUTION) awarded to Andréa Tommasi.

560 **7 Open Research**

561 All data, code, and relevant information for reproducing this work can be found
562 at https://github.com/buchanankerswell/kerswell_et_al_rocmlm, and at <https://doi.org/10.17605/OSF.IO/K23TB>, the official Open Science Framework data repository
563 (Kerswell et al., 2024). All code is MIT Licensed and free for use and distribution (see
564 license details). Reference models PREM and STW105 are freely available from the In-
565 incorporated Research Institutions for Seismology Earth Model Collaboration (IRIS EMC,
566 doi: 10.17611/DP/EMC.1, Trabant et al., 2012). All computations were made using CPUs
568 of a Macbook Pro (2022; M2 chip) with macOS 13.4 and using Python 3.11.4.

569 **8 References**

570 **References**

- 571 Agrusta, R., Goes, S., and van Hunen, J. (2017). Subducting-slab transition-zone
 572 interaction: Stagnation, penetration and mode switches. *Earth and Planetary
 573 Science Letters*, 464:10–23.
- 574 Agrusta, R., Tommasi, A., Arcay, D., Gonzalez, A., and Gerya, T. (2015). How
 575 partial melting affects small-scale convection in a plume-fed sublithospheric
 576 layer beneath fast-moving plates. *Geochemistry, Geophysics, Geosystems*,
 577 16(11):3924–3945.
- 578 Akaogi, M., Ito, E., and Navrotsky, A. (1989). Olivine-modified spinel-spinel transi-
 579 tions in the system mg₂siO₄-fe₂siO₄: Calorimetric measurements, thermochem-
 580 ical calculation, and geophysical application. *Journal of Geophysical Research:
 581 Solid Earth*, 94(B11):15671–15685.
- 582 Akaogi, M., Takayama, H., Kojitani, H., Kawaji, H., and Atake, T. (2007). Low-
 583 temperature heat capacities, entropies and enthalpies of mg₂ siO₄ poly-
 584 morphs, and α - β - γ and post-spinel phase relations at high pressure. *Physics
 585 and Chemistry of Minerals*, 34:169–183.
- 586 Ballmer, M., Schmerr, N., Nakagawa, T., and Ritsema, J. (2015). Compositional
 587 mantle layering revealed by slab stagnation at \sim 1000-km depth. *Science ad-
 588 vances*, 1(11):e1500815.
- 589 Bina, C. and Helffrich, G. (1994). Phase transition clapeyron slopes and transition
 590 zone seismic discontinuity topography. *Journal of Geophysical Research: Solid
 591 Earth*, 99(B8):15853–15860.
- 592 Brown, E. and Lesher, C. (2016). Reebox pro: a forward model simulating melting
 593 of thermally and lithologically variable upwelling mantle. *Geochemistry, Geo-
 594 physics, Geosystems*, 17(10):3929–3968.
- 595 Cagnioncle, A., Parmentier, E., and Elkins-Tanton, L. (2007). Effect of solid flow
 596 above a subducting slab on water distribution and melting at convergent plate
 597 boundaries. *Journal of Geophysical Research: Solid Earth*, 112(B9).
- 598 Cerpa, N., Arcay, D., and Padrón-Navarta, J. (2022). Sea-level stability over geolog-
 599 ical time owing to limited deep subduction of hydrated mantle. *Nature Geo-
 600 science*, 15(5):423–428.
- 601 Cerpa, N., Wada, I., and Wilson, C. (2019). Effects of fluid influx, fluid viscosity,
 602 and fluid density on fluid migration in the mantle wedge and their implications

- for hydrous melting. *Geosphere*, 15(1):1–23.
- Christensen, U. (1995). Effects of phase transitions on mantle convection. *Annual Review of Earth and Planetary Sciences*, 23(1):65–87.
- Čížková, H. and Bina, C. (2013). Effects of mantle and subduction-interface rheologies on slab stagnation and trench rollback. *Earth and Planetary Science Letters*, 379:95–103.
- Connolly, J. (2009). The geodynamic equation of state: what and how. *Geochemistry, geophysics, geosystems*, 10(10).
- Connolly, J. and Kerrick, D. (2002). Metamorphic controls on seismic velocity of subducted oceanic crust at 100–250 km depth. *Earth and Planetary Science Letters*, 204(1-2):61–74.
- Connolly, J. and Khan, A. (2016). Uncertainty of mantle geophysical properties computed from phase equilibrium models. *Geophysical Research Letters*, 43(10):5026–5034.
- Dziewoński, A. and Anderson, D. (1981). Preliminary reference earth model. *Physics of the earth and planetary interiors*, 25(4):297–356.
- Fukao, Y., Widjiantoro, S., and Obayashi, M. (2001). Stagnant slabs in the upper and lower mantle transition region. *Reviews of Geophysics*, 39(3):291–323.
- Gerya, T. and Meilick, F. (2011). Geodynamic regimes of subduction under an active margin: effects of rheological weakening by fluids and melts. *Journal of Metamorphic Geology*, 29(1):7–31.
- Gerya, T. and Yuen, D. (2003). Rayleigh–taylor instabilities from hydration and melting propel ‘cold plumes’ at subduction zones. *Earth and Planetary Science Letters*, 212(1-2):47–62.
- Gibbs, J. (1878). On the equilibrium of heterogeneous substances. *American Journal of Science*, 3(96):441–458.
- Goes, S., Yu, C., Ballmer, M., Yan, J., and van der Hilst, R. (2022). Compositional heterogeneity in the mantle transition zone. *Nature Reviews Earth & Environment*, 3(8):533–550.
- Green, D. (1979). Petrogenesis of mid ocean ridge basalts. *The Earth: its origin, structure and evolution*, pages 200–299.
- Hirose, K. (2002). Phase transitions in pyrolytic mantle around 670-km depth: Implications for upwelling of plumes from the lower mantle. *Journal of Geophysical*

- 636 Research: Solid Earth, 107(B4):ECV–3.

637 Holland, T., Green, E., and Powell, R. (2018). Melting of peridotites through to
638 granites: a simple thermodynamic model in the system kncfmashtocr. *Journal*
639 *of Petrology*, 59(5):881–900.

640 Holland, T. and Powell, R. (2001). Calculation of phase relations involving haplo-
641 granitic melts using an internally consistent thermodynamic dataset. *Journal*
642 *of Petrology*, 42(4):673–683.

643 Holland, T. and Powell, R. (2011). An improved and extended internally consistent
644 thermodynamic dataset for phases of petrological interest, involving a new
645 equation of state for solids. *Journal of metamorphic Geology*, 29(3):333–383.

646 Ishii, T., Huang, R., Fei, H., Koemets, I., Liu, Z., Maeda, F., Yuan, L., Wang, L.,
647 Druzhbin, D., Yamamoto, T., et al. (2018). Complete agreement of the post-
648 spinel transition with the 660-km seismic discontinuity. *Scientific reports*,
649 8(1):6358.

650 Ita, J. and Stixrude, L. (1992). Petrology, elasticity, and composition of the mantle
651 transition zone. *Journal of Geophysical Research: Solid Earth*, 97(B5):6849–
652 6866.

653 Ito, E. (1982). Stability relations of silicate spinels, ilmenites, and perovskite. *High*
654 *pressure research in geophysics*, pages 405–419.

655 Ito, E., Akaogi, M., Topor, L., and Navrotsky, A. (1990). Negative pressure-
656 temperature slopes for reactions forming mgsio₃ perovskite from calorimetry.
657 *Science*, 249(4974):1275–1278.

658 Ito, E. and Katsura, T. (1989). A temperature profile of the mantle transition zone.
659 *Geophysical Research Letters*, 16(5):425–428.

660 Ito, E. and Takahashi, E. (1989). Postspinel transformations in the system mg₂si₄-
661 fe₂si₄ and some geophysical implications. *Journal of Geophysical Research:*
662 *Solid Earth*, 94(B8):10637–10646.

663 Jenkins, J., Cottaar, S., White, R., and Deuss, A. (2016). Depressed mantle disconti-
664 nties beneath iceland: Evidence of a garnet controlled 660 km discontinuity?
665 *Earth and Planetary Science Letters*, 433:159–168.

666 Karato, S., Riedel, M., and Yuen, D. (2001). Rheological structure and deformation
667 of subducted slabs in the mantle transition zone: implications for mantle cir-
668 culation and deep earthquakes. *Physics of the Earth and Planetary Interiors*,

- 669 127(1-4):83–108.
- 670 Karki, B. and Stixrude, L. (1999). Seismic velocities of major silicate and oxide
671 phases of the lower mantle. *Journal of Geophysical Research: Solid Earth*,
672 104(B6):13025–13033.
- 673 Karki, B., Stixrude, L., and Wentzcovitch, R. (2001). High-pressure elastic proper-
674 ties of major materials of earth's mantle from first principles. *Reviews of Geo-*
675 *physics*, 39(4):507–534.
- 676 Katsura, T. and Ito, E. (1989). The system mg₂sio₄-fe₂sio₄ at high pressures and
677 temperatures: Precise determination of stabilities of olivine, modified spinel,
678 and spinel. *Journal of Geophysical Research: Solid Earth*, 94(B11):15663–
679 15670.
- 680 Katsura, T., Yamada, H., Shinmei, T., Kubo, A., Ono, S., Kanzaki, M., Yoneda,
681 A., Walter, M., Ito, E., Urakawa, S., et al. (2003). Post-spinel transition in
682 mg₂sio₄ determined by high p-t in situ x-ray diffractometry. *Physics of the*
683 *Earth and Planetary Interiors*, 136(1-2):11–24.
- 684 Kelley, K., Plank, T., Newman, S., Stolper, E., Grove, T., Parman, S., and Hauri,
685 E. (2010). Mantle melting as a function of water content beneath the mariana
686 arc. *Journal of Petrology*, 51(8):1711–1738.
- 687 Kerswell, B., Cerpa, N., Tommasi, A., Godard, M., and Padrón-Navarta, J. (2024).
688 RocMLMs: Predicting rock properties through machine learning models
689 [dataset repository].
- 690 Kerswell, B., Kohn, M., and Gerya, T. (2021). Backarc lithospheric thickness and
691 serpentine stability control slab-mantle coupling depths in subduction zones.
692 *Geochemistry, Geophysics, Geosystems*, 22(6):e2020GC009304.
- 693 Kuritani, T., Xia, Q., Kimura, J., Liu, J., Shimizu, K., Ushikubo, T., Zhao, D., Nak-
694 agawa, M., and Yoshimura, S. (2019). Buoyant hydrous mantle plume from the
695 mantle transition zone. *Scientific Reports*, 9(1):6549.
- 696 Kustowski, B., Ekström, G., and Dziewoński, A. (2008). Anisotropic shear-wave ve-
697 locity structure of the earth's mantle: A global model. *Journal of Geophysical*
698 *Research: Solid Earth*, 113(B6).
- 699 Le Roux, V., Bodinier, J., Tommasi, A., Alard, O., Dautria, J., Vauchez, A., and
700 Riches, A. (2007). The lherz spinel lherzolite: refertilized rather than pristine
701 mantle. *Earth and Planetary Science Letters*, 259(3-4):599–612.

- 702 Li, Z., Gerya, T., and Connolly, J. (2019). Variability of subducting slab morpholo-
703 gies in the mantle transition zone: Insight from petrological-thermomechanical
704 modeling. *Earth-Science Reviews*, 196:102874.
- 705 Litasov, K., Ohtani, E., Sano, A., Suzuki, A., and Funakoshi, K. (2005). Wet sub-
706 duction versus cold subduction. *Geophysical Research Letters*, 32(13).
- 707 Liu, M., Yuen, D., Zhao, W., and Honda, S. (1991). Development of diapiric struc-
708 tures in the upper mantle due to phase transitions. *Science*, 252(5014):1836–
709 1839.
- 710 Maruyama, S., Liou, J., and Terabayashi, M. (1996). Blueschists and eclogites of the
711 world and their exhumation. *International geology review*, 38(6):485–594.
- 712 Morishima, H., Kato, T., Suto, M., Ohtani, E., Urakawa, S., Utsumi, W., Shimo-
713 mura, O., and Kikegawa, T. (1994). The phase boundary between α -and
714 β -mg2sio4 determined by in situ x-ray observation. *Science*, 265(5176):1202–
715 1203.
- 716 Nakagawa, T. and Buffett, B. (2005). Mass transport mechanism between the upper
717 and lower mantle in numerical simulations of thermochemical mantle convec-
718 tion with multicomponent phase changes. *Earth and Planetary Science Letters*,
719 230(1-2):11–27.
- 720 Pedregosa, F., Varoquaux, G., Gramfort, A., Michel, V., Thirion, B., Grisel, O.,
721 Blondel, M., Prettenhofer, P., Weiss, R., Dubourg, V., Vanderplas, J., Pas-
722 sos, A., Cournapeau, D., Brucher, M., Perrot, M., and Duchesnay, E. (2011).
723 Scikit-learn: Machine learning in Python. *Journal of Machine Learning Re-
724 search*, 12:2825–2830.
- 725 Riel, N., Kaus, B., Green, E., and Berlie, N. (2022). Magemin, an efficient gibbs
726 energy minimizer: application to igneous systems. *Geochemistry, Geophysics,
727 Geosystems*, 23(7):e2022GC010427.
- 728 Ringwood, A. (1991). Phase transformations and their bearing on the constitution
729 and dynamics of the mantle. *Geochimica et Cosmochimica Acta*, 55(8):2083–
730 2110.
- 731 Schubert, G., Yuen, D., and Turcotte, D. (1975). Role of phase transitions in a dy-
732 namic mantle. *Geophysical Journal International*, 42(2):705–735.
- 733 Shaw, D. (1970). Trace element fractionation during anatexis. *Geochimica et Cos-
734 mochimica Acta*, 34(2):237–243.

- 735 Sizova, E., Gerya, T., Brown, M., and Perchuk, L. (2010). Subduction styles in the
736 precambrian: insight from numerical experiments. *Lithos*, 116(3-4):209–229.
- 737 Spear, F. (1993). Metamorphic phase equilibria and pressure-temperature-time
738 paths. *Mineralogical Society of America Monograph*, 799.
- 739 Stixrude, L. and Lithgow-Bertelloni, C. (2005). Thermodynamics of mantle miner-
740 als—i. physical properties. *Geophysical Journal International*, 162(2):610–632.
- 741 Stixrude, L. and Lithgow-Bertelloni, C. (2012). Geophysics of chemical heterogeneity
742 in the mantle. *Annual Review of Earth and Planetary Sciences*, 40:569–595.
- 743 Stixrude, L. and Lithgow-Bertelloni, C. (2022). Thermal expansivity, heat ca-
744 pacity and bulk modulus of the mantle. *Geophysical Journal International*,
745 228(2):1119–1149.
- 746 Sun, S. and McDonough, W. (1989). Chemical and isotopic systematics of oceanic
747 basalts: implications for mantle composition and processes. *Geological Society,*
748 *London, Special Publications*, 42(1):313–345.
- 749 Syracuse, E., van Keken, P., and Abers, G. (2010). The global range of subduction
750 zone thermal models. *Physics of the Earth and Planetary Interiors*, 183(1-
751 2):73–90.
- 752 Tackley, P., Stevenson, D., Glatzmaier, G., and Schubert, G. (1994). Effects of mul-
753 tiple phase transitions in a three-dimensional spherical model of convection in
754 earth’s mantle. *Journal of Geophysical Research: Solid Earth*, 99(B8):15877–
755 15901.
- 756 Tackley, P. and Xie, S. (2003). Stag3d: a code for modeling thermo-chemical multi-
757 phase convection in earth’s mantle. In *Computational Fluid and Solid Mechan-
758 ics 2003*, pages 1524–1527. Elsevier.
- 759 Torii, Y. and Yoshioka, S. (2007). Physical conditions producing slab stagnation:
760 Constraints of the clapeyron slope, mantle viscosity, trench retreat, and dip
761 angles. *Tectonophysics*, 445(3-4):200–209.
- 762 Trabant, C., Hutko, A., Bahavar, M., Karstens, R., Ahern, T., and Aster, R. (2012).
763 Data products at the iris dmc: Stepping stones for research and other applica-
764 tions. *Seismological Research Letters*, 83(5):846–854.
- 765 Wang, X., Wilde, S., Li, Q., and Yang, Y. (2015). Continental flood basalts derived
766 from the hydrous mantle transition zone. *Nature Communications*, 6(1):7700.

- 767 Waszek, L., Tauzin, B., Schmerr, N., Ballmer, M., and Afonso, J. (2021). A poorly
768 mixed mantle transition zone and its thermal state inferred from seismic
769 waves. *Nature Geoscience*, 14(12):949–955.
- 770 Workman, R. and Hart, S. (2005). Major and trace element composition of the de-
771 pleated morb mantle (dmm). *Earth and Planetary Science Letters*, 231(1-2):53–
772 72.
- 773 Xu, W., Lithgow-Bertelloni, C., Stixrude, L., and Ritsema, J. (2008). The effect of
774 bulk composition and temperature on mantle seismic structure. *Earth and*
775 *Planetary Science Letters*, 275(1-2):70–79.
- 776 Yang, J. and Faccenda, M. (2020). Intraplate volcanism originating from upwelling
777 hydrous mantle transition zone. *Nature*, 579(7797):88–91.